

Short Communication

Preparation of Pd-Co Bimetallic Nanoparticles Supported on Graphene for Rapid Electrochemical Detection of Nitrite

Jinlan Jiang*, Shijian Bao, Jun Lv, Xinping Yu

School of Intelligent Manufacturing, Zhejiang Guangsha Vocational and Technical University of Construction, Dongyang, Zhejiang, 322100, P.R. China

*E-mail: jinlanjiang2018@163.com

Received: 5 September 2021 / Accepted: 26 October 2021 / Published: 6 December 2021

Nitrite has been widely used in industrial and agricultural production and commonly exists in food, drinking water, organisms and the environment. However, nitrite is a toxic contaminant that can be very harmful to humans. In recent years, various methods for detecting nitrite have been developed, among which electrochemical methods are favored for their simplicity, rapidity, sensitivity and low price. In this paper, a graphene supported nano-PdCo alloy catalyst is proposed for the preparation of electrochemical nitrite sensor. The results show that the as-prepared sensor has a good electrocatalytic effect on the detection of nitrite. The electrochemical sensor can be adopted for rapid detection of nitrite with a wide range of 20~1050 μM and the low detection limit of 7.7 nM. The proposed sensor has been successfully applied to the detection of nitrite in pure water, with the recovery rate being 99.17% to 107.24%, which indicates that the sensor has good stability and reproducibility.

Keywords: Bimetallic Nanoparticle, Electrochemical sensor; Nitrite; Graphene; Nanocatalysts

1. INTRODUCTION

Nitrite can be commonly found in food, drinking water and the environment, mainly from livestock manure, organic waste, chemical fertilizers, natural deposits and other nitrogen-containing organic matter [1,2]. Nitrite can interact with proteins to produce highly carcinogenic nitrosamines. Excessive intake of nitrite can cause many health problems, such as stomach and esophageal cancers, methemoglobinemia in infants, and birth defects of central nervous system. Many countries and organizations have established maximum limits for nitrite in the environment [3,4]. The U.S. National Environmental Protection Agency has set a limit of 1 ppm (21.7 mM), the European Union Scientific Committee on Food has set the daily intake of nitrite at 0.06 mg/kg, and the Chinese national standard GB 2760-2014 has set the maximum use of nitrite as a preservative in cured meat and marinated meat at 0.15 g/kg.

Nitrite levels are required for food safety monitoring, food analysis and water quality analysis [5]. Many nitrite detection methods have been reported in the literature, such as spectrophotometric methods (e.g. Griess reaction, etc.) [6], chemiluminescence [7], chromatography [8], surface-enhanced Raman spectroscopy [9], capillary electrophoresis [10], fluorescence [11] and electrochemiluminescence [12]. However, these testing processes are complex and time-consuming. Electrochemical detection methods have the advantages of being simple, rapid, sensitive, and inexpensive [13,14], and nitrite is an electrically active substance on the surfaces of platinum, gold, copper, glassy carbon and transition metal oxide electrodes [15]. However, the electrode surface is susceptible to contamination, which reduces the sensitivity and accuracy of the detection and to some extent limits the practical application of bare electrodes for nitrite detection [16]. The necessary modification of the electrode surface can not only increase the response signal of the oxidation reaction of nitrite, but also broaden the kinetic range of detection.

Graphene is an emerging carbon material with excellent electrical properties, thermal stability and large specific surface area, making it an ideal carrier for nanocatalysts and attracting widespread attention in the field of nanocatalysis [17–19]. Monometallic nanocrystals are most commonly selected among nanocatalysts. Compared with monometallic nanocrystals, bimetallic nanocrystals exhibit a number of unique properties. When transition metals are introduced into noble metal nanoparticles, the catalytic activity, selectivity and stability can be enhanced by the synergistic effect among metals [20–22]. Therefore, an increasing number of studies have focused on the preparation of bimetallic nanocrystals of noble metals and transition metals to reduce the amount of noble metals without destroying the original activity. For example, the alloy made of the mixture of the noble metal Au and the transition metal (Fe, Co, Ni) can reduce the amount of Au, and the respective properties of each metal can be enhanced [23,24].

The aim of this work is to explore the preparation of graphene supported bimetallic alloy catalysts and to enhance the electrocatalytic activity of the catalysts by applying the synergistic interaction between bimetallic nanoparticles and graphene. In this work, an electrochemical sensor was constructed for nitrite based on Au-Co/reduced graphene oxide (rGO) composite modified with glassy carbon electrode (GCE). This work also investigated the electrochemical behavior of nitrite on the surface of this composite electrode. In addition, the performance of the sensor for nitrite was also investigated in the presence of interfering substances such as sodium nitrate, copper sulfate, sodium chloride, urea, glucose, nickel chloride, and potassium chloride.

2. MATERIALS AND METHODS

Materials: $\text{Co}(\text{C}_4\text{H}_6\text{O}_4)\cdot 4\text{H}_2\text{O}$, potassium ferricyanide, potassium ferrocyanide, ammonia, and hydrazine hydrate were purchased from Sinopharm Group Chemical Reagent Co. PdCl_2 was purchased from Nanjing Jingrui Jiu'an Biotechnology Co. Graphene oxide (GO) was purchased from Xianfeng Nanotech Co.

Instruments: All electrochemical tests were carried out with a CHI620E workstation. X-ray diffraction (XRD) was determined on a D/MAX2500V X-ray diffractometer. Raman spectroscopy was

performed on a LABRAM-HR Raman spectroscopy. The analysis was performed at ambient temperature with a 514.5 nm laser. Field emission transmission electron microscopy (TEM) analysis was performed with a JEOL JEM-2100F.

Preparation of Pd-Co/rGO bimetallic modifier: A solution of 0.282 mM PdCl₂ and 0.282 mM Co(C₄H₆O₄) •4H₂O solids was weighed and fixed at 50 mL. The prepared solution was then mixed with graphene oxide solution (0.2 mg/mL) and stirred magnetically for 1 h. After mixing and stirring, 50 mL of ammonia was slowly added to the solution to adjust the pH=10, and then 35 mL of hydrazine hydrate solution with a mass concentration of 85% was added and the reaction was carried out for 4 h at 80 °C. A black precipitate could be observed in the solution. After the reaction, the black solid was obtained by centrifugation and washed with deionized water to neutral. Afterwards, the solid was dried under vacuum at 60°C to obtain a black flaky solid, which was ground to obtain a uniform black powder. The black powder was laid flat on a quartz boat, placed in the constant temperature zone of the tube furnace, heated up to 300°C under nitrogen atmosphere (flow rate of 600 mL/min), fed with hydrogen gas (flow rate of 100 mL/min), reduced and calcined for 120 min, and cooled to room temperature under nitrogen gas protection. The Pd-Co/rGO was obtained by heating up it to 500°C under nitrogen atmosphere (flow rate of 600 mL/min), reducing and calcining it with hydrogen gas (flow rate of 100 mL/min) for 120 min, and cooling it to room temperature under nitrogen protection.

Electrochemical sensing: The bare GCE was polished with 1.0 μm, 0.3 μm and 0.05 μm alumina powder on a chamois. The electrodes were then sonicated in distilled water, anhydrous ethanol and distilled water for 10s each. The electrodes were scanned for several revolutions (scanning voltage ranges from -0.2 V to 0.8 V) by cyclic voltammetry in 5 mM potassium ferricyanide/potassium ferrocyanide solution of electrolyte until a stable current-potential curve with a peak potential difference within 100 mV was obtained. Afterwards, a certain amount of Pd-Co/rGO was drop coated on the GCE and dried naturally. In real sample test, tap water was selected as the actual sample for the spiked recovery of nitrite. The tap water was filtered with a 0.45 μm membrane and the filtrate was collected and added with a known amount of nitrite. Cyclic voltammetry has been adopted for nitrite sensing. The scan window was between 0.3 to 1.2 V and the scan rate was 50 mV/s.

3. RESULTS AND DISCUSSION

Figure 1 shows the TEM image of the Pd-Co/rGO. The size, morphology and dispersion of the Pd-Co/rGO can be obtained. In Figure 1A, it can be seen that the nearly transparent background is graphene. The surface of graphene has many folds that are disordered, and a large number of spherical nanoalloy particles are uniformly loaded on the surface with little agglomeration. Despite that the composites were prepared after a long period of ultrasonic exfoliation, no free alloy nanoparticles were found outside the graphene, which indicates that there is a strong interaction between the alloy nanoparticles and the graphene surface [25]. The size of the Pd-Co alloy was counted, and it was concluded that the particle size of the Pd-Co alloy ranged from 5 to 20 nm, with an average particle size of 11.51 ± 0.8 nm (Figure 1B).

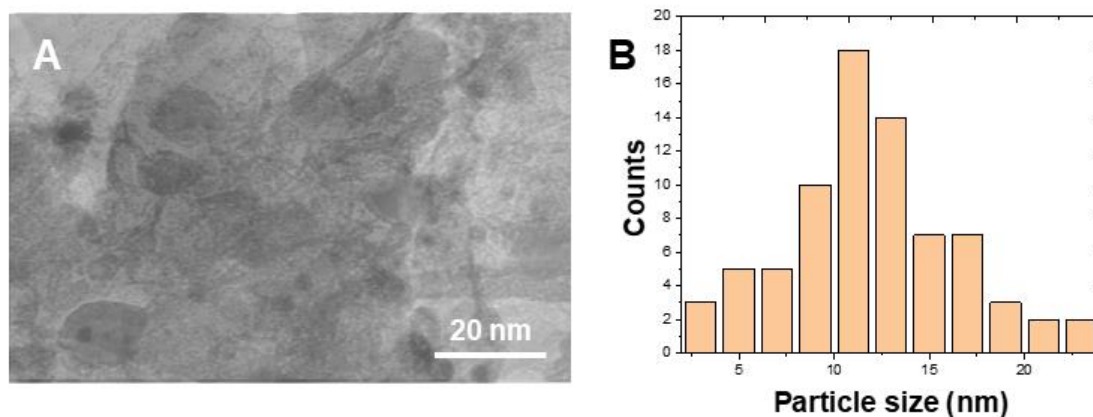


Figure 1. (A) TEM image of Pd-Co/rGO. (B) Size distribution of Pd-Co alloy particles.

Figure 2A shows that the XRD pattern of Pd-Co/rGO. It can be noted that with the reduction of GO, the (001) characteristic diffraction peak of graphite oxide disappears. The position of the peak shifts up to around $2\theta=26^\circ$, which indicates that the graphite oxide has been reduced and has regained its ordered crystal structure [26]. $2\theta=40.08^\circ$, 46.77° , 68.17° and 82.15° peaks (JCPD-46-1043) are for the monolithic palladium (111), (200), (220), (311) characteristic peaks [27]. $2\theta=44.48^\circ$, 47.33° (JCPD-15-0806) are the characteristic peaks of monolithic cobalt [28]. The amorphous structure of the precursor was observed to convert into the crystal structure [29].

Raman spectroscopy has been widely used in the characterization of carbon materials, and is an important method to characterize graphene and its derivatives by determining the sp^2 and sp^3 hybridized carbon atoms in the material and their internal structural features. Figure 2B presents the Raman spectra of GO and Pd-Co/rGO [30]. It can be seen that there are two characteristic peaks in the range of $1000-2000\text{ cm}^{-1}$ in GO, among which the characteristic peak at 1353 cm^{-1} is usually called the D-band, which is a disorder-induced Raman feature of carbon material due to the defect disorder in the lattice [31]. As long as there is a disorder arrangement in the carbon material, the D-band will be generated in the Raman spectrum. The characteristic peak at the 1603 cm^{-1} position is the intrinsic Raman mode of graphite, called the G-band, which arises due to the scattering of E_{2g} phonon vibrations in the center of the Brillouin zone [32]. Comparing the Raman spectra of Pd-Co/rGO and GO, two characteristic peaks of GO are also present in the reduced Pd-Co/rGO. The intensity ratio (I_D/I_G) of peak D and peak G is usually adopted to reflect the graphitization degree and defect degree of carbon materials [33]. The intensity of the peaks in both D-band and G-band decreases after the reduction, indicating that the disordered structure of GO was repaired after the reduction. The ratio of $I_{(D)}/I_{(G)}$ was compared between the two, where GO ($I_{(D)}/I_{(G)} = 0.91$) is significantly lower than Pd-Co/rGO ($I_{(D)}/I_{(G)} = 1.47$), which is possibly resulted from the reconversion of the sp^3 hybridization of carbon atoms in graphene oxide to sp^2 hybrid structure after reduction [34]. However, the ratio of the D and G peaks increases due to the gradual decrease of the average region of sp^2 carbon atoms. These results indicate that the graphite oxide has been reduced and the original ordered structure and sp^2 hybridization have been restored.

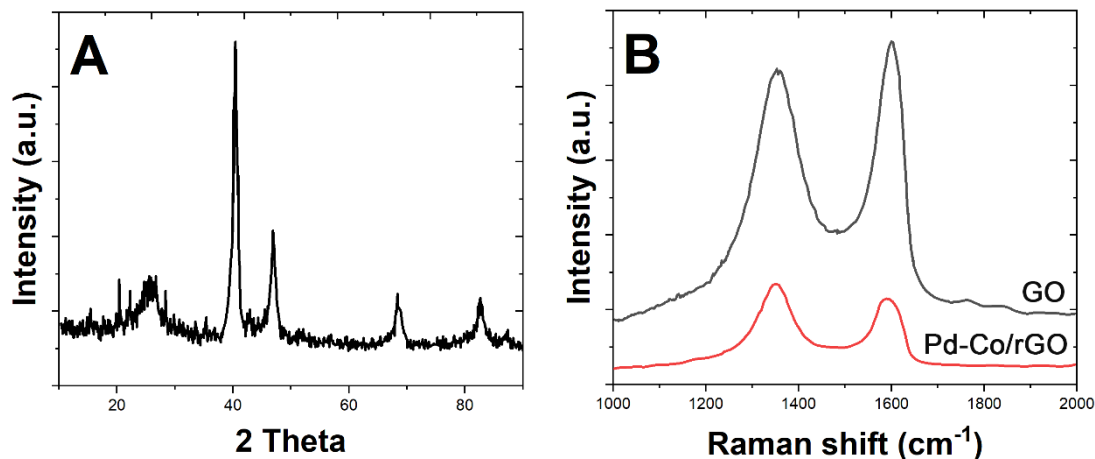


Figure 2. (A) XRD pattern of Pd-Co/rGO. (B) Raman spectra of GO and Pd-Co/rGO.

The evaluation of the electrical properties of the sensors was characterized by cyclic voltammetry. Figure 3A shows the comparison of cyclic voltammetry curves induced by Pd-Co/rGO/GCE and bare GCE in the background of potassium ferricyanide and potassium ferrocyanide (sweep speed 100 mV/s). As shown in the figure, both the bare GCE and the modified electrode induce a pair of obvious redox peaks, and the ratio of the induced oxidation peak current to the reduction peak current value is close to 1, which indicates that the redox reaction is reversible in this system. The reason for this is the reversible one-electron redox behavior of ferricyanate and ferrocyanide ions at the electrode surface. The smaller the potential difference is, the higher the redox peak current is, indicating the better electrical performance of the sensor [35]. The cyclic voltammetric response signal corresponding to the bare GCE shows a significantly larger potential difference and smaller peak current values than that of Pd-Co/rGO/GCE. Therefore, the Pd-Co/rGO modified electrode shows a great improvement in electrical performance relative to the bare GCE.

Figure 3B presents a comparison of the EIS curves of Pd-Co/rGO/GCE and bare GCE in $\text{Fe}(\text{CN})_6^{3-/4-}$. The Nyquist plot generally consists of two parts: a semicircular part at high frequency and a linear part at low frequency. The semicircle at high frequency represents the charge transfer control process and the diameter of the semicircle represents the magnitude of the charge transfer resistance R_{ct} , which controls the charge transfer kinetics in the redox reaction at the electrode surface. The curve corresponding to bare GCE shows a larger semicircle diameter, and by fitting the appropriate circuit, the R_{ct} is 171 Ω . Pd-Co/rGO/GCE has a smaller semicircle diameter, and the R_{ct} value is 77 Ω . Compared with bare GCE, the R_{ct} value corresponding to Pd-Co/rGO/GCE is greatly reduced, which indicates that the modified material accelerates the electron transfer rate between the $\text{Fe}(\text{CN})_6^{3-/4-}$ probe molecule and the electrode surface. Moreover, it also means that the conductivity of the sensor is greatly improved, which is consistent with the results obtained by cyclic voltammetry.

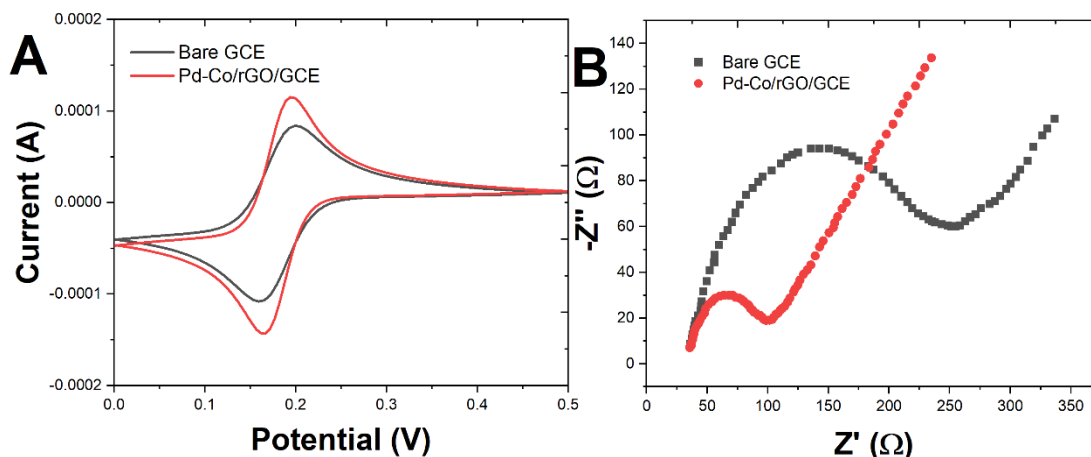


Figure 3. (A) CVs and (B) EIS of bare GCE and Pd-Co/rGO/GCE in a solution which contains 5mM $K_3Fe(CN)_6$, 5 mM $K_4Fe(CN)_6$ and 0.1 M KCl (Scan rate is 100 mV/s).

In this study, the electrocatalytic performance of the sensor was tested mainly by cyclic voltammetry. Figure 4A shows the CV sensing of Pd-Co/rGO/GCE in PBS buffer solution containing 20 μ M nitrite, and blank PBS buffer solution, respectively. It can be seen that a very distinct irreversible oxidation peak appears at around 0.95 V during the scan, which is resulted from the oxidation of nitrite at this potential where an oxidation peak appears. Considering the absence of a peak in the blank solution, this indicates that the sensor has electrocatalytic nitrite oxidation performance and can catalyze the nitrite reaction to produce nitrate.

PH is an important property of electrolytes, which has a significant effect on the response signal of the sensor. The Pd-Co/rGO/GCE was subjected to cyclic voltammetric scanning in 0.1 M PBS with different pH. As shown in the Figure 4B, the oxidation peak current increases gradually as the pH increases from 3 to 7. The strongest response signal of the sensor appears when the electrolyte is neutral, while the response current gradually decreases again as the electrolyte is alkaline, which indicates that the catalytic effect of Pd-Co/rGO/GCE on nitrite is most pronounced under neutral conditions. Therefore, the electrolyte 0.1 M PBS prepared in pH 7.0 was chosen.

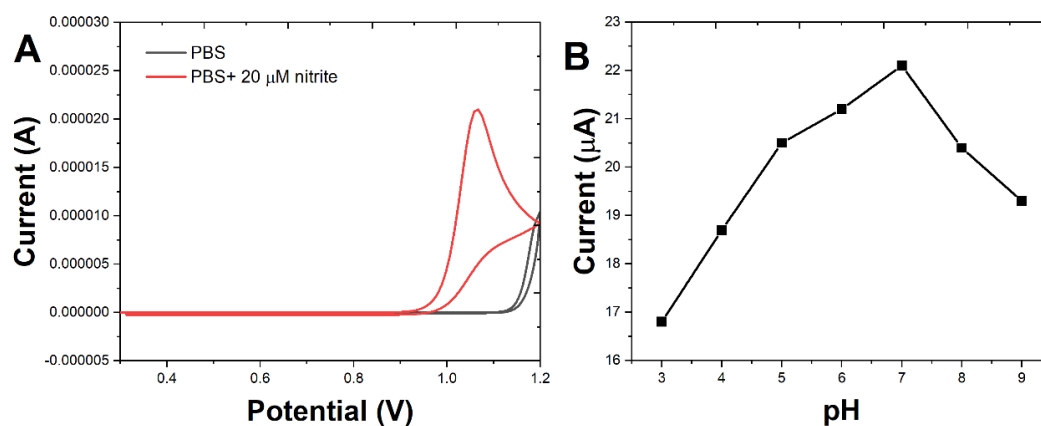


Figure 4. (A) CV responses of Pd-Co/rGO/GCE in blank and 20 μ M $NaNO_2$ contained 0.1 M PBS (pH = 7). (B) The effect of pH values on the CV response of Pd-Co/rGO/GCE toward 20 μ M nitrite in 0.1 M PBS.

In this experiment, cyclic voltammetry and constant potential methods were adopted to detect trace amounts of nitrite. The cyclic voltammetric response curves of Pd-Co/rGO/GCE for the detection of different concentrations of nitrite are shown in Figure 5A, from which it can be seen that the cyclic voltammetric response oxidation peak current increases gradually as the concentration of nitrite increases from 5 μM to 100 μM , being increasingly significant. The reason for this phenomenon is that the larger the concentration of nitrite is, the stronger the Pd-Co/rGO/GCE-induced electrical response signal is.

Figure 5B reveals that the response current shows a good linear relationship with the nitrite concentration, which is in the range of 20 μM to 1050 μM with the response current reaching 0.9894. The lower limit of detection is 7.7 nM. Table 1 shows the comparison between the sensing properties of Pd-Co/rGO/GCE with reported nitrite sensors in literature. It is found from Table 1 that the sensitivity and detection limit of Pd-Co/rGO is better than other nitrite sensors, indicating that there are more stable and more active electrochemical sites on nanostructured Pt-Co surface.

Table 1. Comparison between the sensing properties of Pd-Co/rGO/GCE with reported nitrite sensors in literature

Sensor	Linear range	Limit of detection	Ref.
Au Cu NCN	10-400 μM	0.2 μM	[36]
Au ₂ Pt ₁ NPs/PyTs-NG	0.5-162 μM	0.19 μM	[37]
AuNPs/Ti ₃ C ₂ TX	1-458 μM	0.14 μM	[38]
Nafio/Hb/MXene-Ti ₃ C ₂	0.5-1180 μM	0.12 μM	[39]
Pd-Co/rGO	20-100 μM	7.7 nM	This work

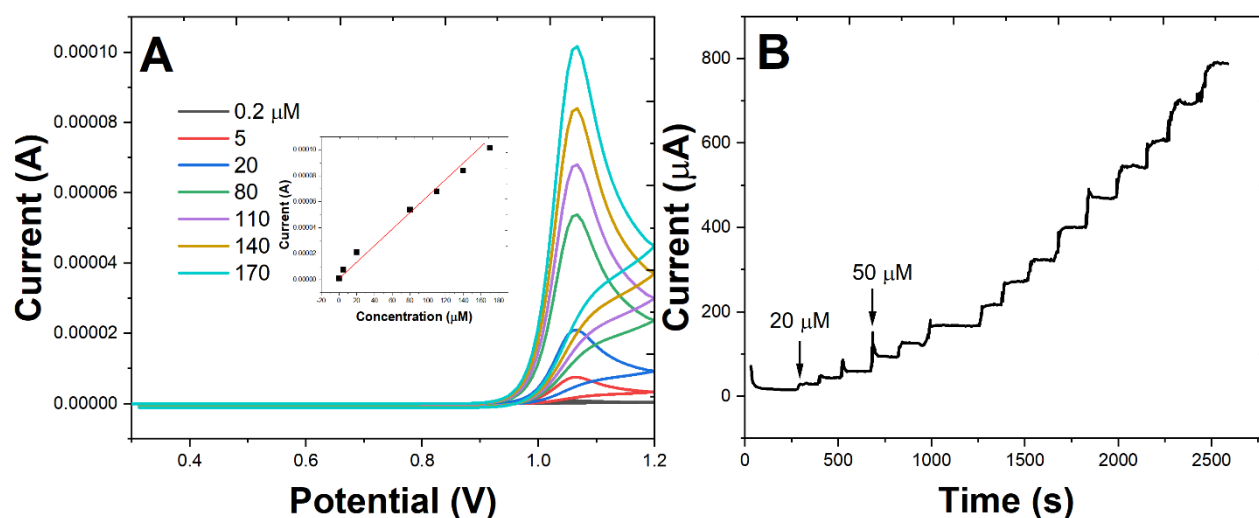


Figure 5. (A) CV response curves of Pd-Co/rGO/GCE toward different concentrations of nitrite in 0.1 M PBS (Inset: calibration curve). (B) I-t curve at a constant voltage of 0.95 V with the successive addition of different concentrations of nitrite onto the Pd-Co/rGO/GCE.

The anti-interference of Pd-Co/rGO/GCE to interference during the detection of nitrite electrodes was further investigated in this study. No significant change in the oxidation peak current of nitrite appeared in the presence of 0.1 M of NO_3^- , Cu_2^+ , Na^+ , K^+ , Ni_2^+ , SO_4^{2-} , urea and glucose, which indicates that the above-mentioned cations as well as oxygenated anions do not interfere with the nitrite electrochemical sensor in the process of detection, meaning that the nitrite electrochemical sensor has good immunity to interference in the process of detection.

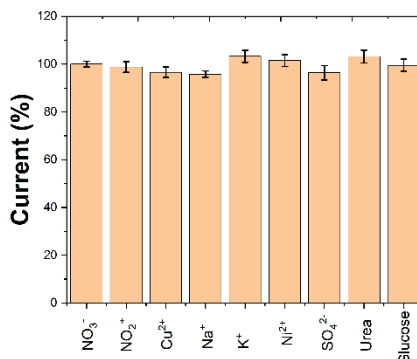


Figure 6. Interference study of the Pd-Co/rGO/GCE for nitrite sensing in the presence of NO_3^- , Cu^{2+} , Na^+ , K^+ , Ni^{2+} , SO_4^{2-} , urea and glucose.

In order to further test the feasibility of the sensor for detecting nitrite, the actual sample of drinking water was selected for spiking and recovery test in this experiment. The result of spiked recovery test in the water sample is shown in Table 2, from which it can be noted that the recovery is between 99.17% to 107.24%, indicating that the sensor can be used directly for the detection of nitrite in freshwater with a good accuracy.

Table 2. Standard addition test of nitrite in drinking water using Pd-Co/rGO/GCE.

Sample	Detection (μM)	Added (μM)	Detection (μM)	Recovery (%)
1	0.00	30.00	29.75	99.17
2	0.00	50.00	52.21	104.42
3	0.00	100.00	107.24	107.24

4. CONCLUSIONS

In conclusion, in this study a Pd-Co/rGO/GCE as electrochemical sensor was prepared for rapid detection of nitrite and rGO supported bimetallic alloy catalysts can enhance the electrocatalytic activity of the sensor through the synergistic interaction. The Pd-Co/rGO/GCE shows an excellent performance

towards nitrite oxidation. Under optimum condition, the proposed sensor can linearly detect nitrite in the range of 20 μM to 1050 μM with a low limit of detection being 7.7 nM.

References

1. Mounesh, K.R. Venugopala Reddy, *Anal. Chim. Acta*, 1108 (2020) 98–107.
2. M. Annalakshmi, R. Balaji, S.-M. Chen, T.-W. Chen, Y.C. Huang, *Electrochimica Acta*, 360 (2020) 136797.
3. K.N. Nithyayini, M.N.K. Harish, K.L. Nagashree, *Electrochimica Acta*, 317 (2019) 701–710.
4. L. Cao, Z.-W. Kang, Q. Ding, X. Zhang, H. Lin, M. Lin, D.-P. Yang, *Sci. Total Environ.*, 723 (2020) 138008.
5. H. Chen, T. Yang, F. Liu, W. Li, *Sens. Actuators B Chem.*, 286 (2019) 401–407.
6. K. Lin, J. Xu, X. Dong, Y. Huo, D. Yuan, H. Lin, Y. Zhang, *Microchem. J.*, 158 (2020) 105272.
7. S. Han, X. Chen, *Spectrochim. Acta. A. Mol. Biomol. Spectrosc.*, 210 (2019) 315–320.
8. B.W. Pirok, D.R. Stoll, P.J. Schoenmakers, *Anal. Chem.*, 91 (2018) 240–263.
9. A.I. Pérez-Jiménez, D. Lyu, Z. Lu, G. Liu, B. Ren, *Chem. Sci.*, 11 (2020) 4563–4577.
10. Ö.Ö. Erol, B.Y. Erdoğan, A.N. Onar, *J. Forensic Sci.*, 62 (2017) 423–427.
11. B.-L. Li, Y.-S. Li, X.-F. Gao, *Food Chem.*, 274 (2019) 162–169.
12. Q.-H. Wang, L.-J. Yu, Y. Liu, L. Lin, R. Lu, J. Zhu, L. He, Z.-L. Lu, *Talanta*, 165 (2017) 709–720.
13. G. Kaladevi, P. Wilson, K. Pandian, *J. Electrochem. Soc.*, 167 (2020) 027514.
14. T. Zhe, R. Li, Q. Wang, D. Shi, F. Li, Y. Liu, S. Liang, X. Sun, Y. Cao, L. Wang, *Sens. Actuators B Chem.*, 321 (2020) 128452.
15. S.-S. Chen, Y.-C. Shi, A.-J. Wang, X.-X. Lin, J.-J. Feng, *J. Electroanal. Chem.*, 791 (2017) 131–137.
16. C. Li, D. Chen, Y. Wang, X. Lai, J. Peng, X. Wang, K. Zhang, Y. Cao, *Sensors*, 19 (2019) 1304.
17. L. Fu, A. Wang, G. Lai, W. Su, F. Malherbe, J. Yu, C.-T. Lin, A. Yu, *Talanta*, 180 (2018) 248–253.
18. H. Karimi-Maleh, F. Karimi, L. Fu, A.L. Sanati, M. Alizadeh, C. Karaman, Y. Orooji, *J. Hazard. Mater.*, 423 (2022) 127058.
19. H. Karimi-Maleh, Y. Orooji, F. Karimi, M. Alizadeh, M. Baghayeri, J. Rouhi, S. Tajik, H. Beitollahi, S. Agarwal, V.K. Gupta, *Biosens. Bioelectron.* (2021) 113252.
20. M. Mann, G. Beach, *APL Mater.*, 5 (2017) 106104.
21. G. Rochard, J.-M. Giraudon, L.F. Liotta, V. La Parola, J.-F. Lamonier, *Catal. Sci. Technol.*, 9 (2019) 3203–3213.
22. S. Wei, X. Chen, X. Zhang, L. Chen, *Front. Chem.*, 9 (2021) 697.
23. Z. Wu, J. Liu, M. Liang, H. Zheng, C. Zhu, Y. Wang, *Front. Chem.*, 9 (2021) 208.
24. W.-C. Lee, K.-B. Kim, N. Gurudatt, K.K. Hussain, C.S. Choi, D.-S. Park, Y.-B. Shim, *Biosens. Bioelectron.*, 130 (2019) 48–54.
25. D. Yang, W. Hou, Y. Lu, W. Zhang, Y. Chen, *Nanoscale*, 11 (2019) 12837–12845.
26. M.G. Hosseini, F. Hosseinzadeh, P. Zardari, M. Darbandi, *Int. J. Hydrog. Energy*, 46 (2021) 28513–28526.
27. B. Qu, Y. Tao, L. Yang, Y. Liu, *Int. J. Hydrog. Energy*, 46 (2021) 31324–31333.
28. S. Shahrokhian, S. Rezaee, *Electroanalysis*, 29 (2017) 2591–2601.
29. D.E. Karakaş, M. Akdemir, A. Atabani, M. Kaya, *Fuel*, 304 (2021) 121334.
30. A. Ehsani, A. Heidari, R. Asgari, *Chem. Rec.*, 19 (2019) 2341–2360.
31. R. Saraswathy, R. Suman, P.M. Bruntha, D. Khanna, V. Chellasamy, *RSC Adv.*, 11 (2021) 28829–28837.

32. M.E. Assal, M.R. Shaik, M. Kuniyil, M. Khan, A. Al-Warthan, A.I. Alharthi, R. Varala, M.R.H. Siddiqui, S.F. Adil, *Arab. J. Chem.*, 12 (2019) 54–68.
33. B. Qu, Y. Tao, L. Yang, Y. Liu, *Int. J. Hydrog. Energy*, 46 (2021) 31324–31333.
34. I. Maity, D. Acharyya, K. Huang, P. Chung, M. Ho, P. Bhattacharyya, *IEEE Trans. Electron Devices*, 65 (2018) 3528–3534.
35. L. Li, H. Zheng, L. Guo, L. Qu, L. Yu, *Talanta*, 197 (2019) 68–76.
36. S.-S. Huang, L. Liu, L.-P. Mei, J.-Y. Zhou, F.-Y. Guo, A.-J. Wang, J.-J. Feng, *Microchim. Acta*, 183 (2016) 791–797.
37. Z. Li, Z. An, Y. Guo, K. Zhang, X. Chen, D. Zhang, Z. Xue, X. Zhou, X. Lu, *Talanta*, 161 (2016) 713–720.
38. H. Zou, F. Zhang, H. Wang, J. Xia, L. Gao, Z. Wang, *New J. Chem.*, 43 (2019) 2464–2470.
39. H. Liu, C. Duan, C. Yang, W. Shen, F. Wang, Z. Zhu, *Sens. Actuators B Chem.*, 218 (2015) 60–66.

© 2022 The Authors. Published by ESG (www.electrochemsci.org). This article is an open access article distributed under the terms and conditions of the Creative Commons Attribution license (<http://creativecommons.org/licenses/by/4.0/>).